STRUCTURAL SCIENCE CRYSTAL ENGINEERING MATERIALS

ISSN 2052-5206

Crystal engineering of co-crystal of nicotinic acid and pyrogallol: an experimental and theoretical electron density analysis

Alia Iqbal,[a] Arshad Mehmood,[b] Sajida Noureen,[a] Claude Lecomte[c,d] and Maqsood Ahmed[a]*

[a]Materials Chemistry Laboratory, Institute of Chemistry, The Islamia University of Bahawalpur, Baghdad-ul-Jadeed Campus, 63100, Pakistan, [b]Department of Chemistry and Biochemistry, Texas Christian University, Fort Worth, Texas 76129, USA, [c]Université de Lorraine, Laboratoire CRM2, UMR CNRS 7036, Boulevard des aiguillettes BP70239, Vandoeuvre-les-Nancy, 54506, France, and [d]CNRS, Laboratoire CRM2, UMR CNRS 7036, Boulevard des aiguillettes BP70239, Vandoeuvre-les-Nancy, 54506, France. *Correspondence e-mail: maqsood.ahmed@iub.edu.pk

Received 29 May 2021
Accepted 3 September 2021

Edited by P. Macchi, Politecnico di Milano, Italy

Keywords: cocrystal; charge density; *MoPro*; nicotinic acid; pyrogallol; crystal engineering.

CCDC references: 2107343; 2107344; 2107345

Supporting information: this article has supporting information at journals.iucr.org/b

Experimental electron density analysis by means of high-resolution X-ray diffraction data up to $\sin\theta/\lambda_{max}$ = 1.11 Å^{-1} at 100 (1) K has been performed to analyze the detailed structure and the strength of intermolecular interactions responsible for the formation of a new solid form of nicotinic acid (NA), cocrystallized with pyrogallol (PY). There are two NA–PY units in the asymmetric unit. The experimental results are compared with the results obtained from theoretical structure factors modeled using periodic boundary DFT calculations. Both refinements were carried out using the Hansen and Coppens multipolar formalism (in *MoPro* program). The non-centrosymmetric and polar nature of the crystal system rendered the multipolar refinement challenging which was addressed by involving the transferability principle. This study highlights the significance of the transferability principle in electron density modeling in non-routine situations. The 2:2 cocrystal of NA–PY exhibits a zigzag, brickwall and sheet-like layered structure in three dimensions and is stabilized by strong intra- and inter-molecular hydrogen bonding through N—H···O and O—H···O bonds, some of them due to the zwitterion nature of NA as well as weak interactions between the PY molecules. Ranking these interactions via topological analysis of the electron density shows the leading role of the NA–NA substructure which drives the organization of the cocrystals. These strong interactions between the NA zwitterions may explain why Z' = 2.

1. Introduction

The experimental charge density analysis, based on low-temperature high-resolution X-ray diffraction, is a reliable tool for the study of both inter- and intra-molecular interactions in crystalline solid state materials (Koritsanszky *et al.*, 1998; Koritsanszky & Coppens, 2001; Jelsch *et al.*, 1998; Lecomte *et al.*, 2004; Fournier *et al.*, 2009; Stalke & Ott, 2008). To predict the nature of chemical bonding in any molecule, to precisely evaluate the interactions between drug and receptor sites and understand molecular recognition at electronic level, charge density analysis provides the ultimate solution (Housset *et al.*, 2000; Muzet *et al.*, 2003; Li *et al.*, 2002; Grabowsky *et al.*, 2009; Destro *et al.*, 2005; Flaig *et al.*, 2001; Guillot *et al.*, 2001; Stalke, 2011; Flierler *et al.*, 2011). The knowledge of charge density distribution is valuable for drug designing through crystal engineering approaches (Duggirala *et al.*, 2016). The topological study of electron density of hydrogen-bonding interactions allows characterizing their

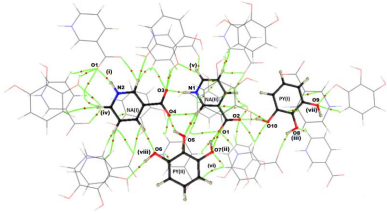

relative strength (Bader, 1990, 1998; Koch & Popelier, 1995; Popelier, 1998; Abramov *et al.*, 1998; Espinosa *et al.*, 1998, 1999; Steiner, 2003; Munshi & Guru Row, 2005; Chopra *et al.*, 2006, 2010). Charge density analysis requires crystals diffracting at very high resolution and ideally in a centrosymmetric space group for better solution of the phase problem. For crystals diffracting to ordinary resolution, the transferability principle (Brock *et al.*, 1991; Pichon-Pesme *et al.*, 1995) can be used to estimate the electron-density-derived properties. There have been numerous studies in the literature where the principle has been successfully applied (Pichon-Pesme *et al.*, 1995; Domagała *et al.*, 2012; Jelsch *et al.*, 1998; Zarychta *et al.*, 2007; Dittrich *et al.*, 2004, 2006*a*,*b*, 2009; Volkov *et al.*, 2007).

Structural investigations up to subatomic level via experimental and theoretical charge density analysis of pharmaceutical cocrystals such as piroxicam–saccharin (Du *et al.*, 2016), paracetamol–4,4′-bipyridine (Du *et al.*, 2018), betaines–*p*-hydroxybenzoic acid cocrystal (Owczarzak & Kubicki, 2018), melamine–barbital (Gryl *et al.*, 2015), isonicotinamide–monofluorobenzoic acids (Hathwar *et al.*, 2011), nicotinamide–salicylic acid–oxalic acid (Hathwar *et al.*, 2010), sulfamethizole–oxalates/sulfates (Thomas *et al.*, 2015), 8-hydroxyquinoline–salicylic acid (Nguyen *et al.*, 2012) *etc.*, have been carried out. These reports describe the importance of charge density analysis for understanding their mechanism of binding inside biological systems.

Two or more components bound together through noncovalent interactions in a crystal structure are termed cocrystals (Desiraju, 2003; Bond, 2007); if one of the components is an active pharmaceutical ingredient (API), then it is defined as pharmaceutical cocrystal (Sekhon, 2009; Karimi-Jafari *et al.*, 2018; Qiao *et al.*, 2011; Prasad *et al.*, 2012; Duggirala *et al.*, 2016; Brittain, 2012). This procedure allows the pharmaceutical industry to bring drugs having enhanced efficacy into the market through different solid forms with improved properties. The improvement of physicochemical properties of API without changing its biological activity is a target research area, equally important for both academic and pharmaceutical industry (Sekhon, 2012).

The crystal structure of 3-pyridine carboxylic acid (nicotinic acid or NA), which is also called vitamin B_3 or niacin (Budavari *et al.*, 1989) was first determined by Wright & King (1950) and refined by Kutoglu & Scheringer (1983). NA is available as a vitamin supplement and used as a drug for the treatment of coronary heart diseases (Malik & Kashyap, 2003). It is primarily used for the treatment of high cholesterol along with many other pharmaceutical benefits (Carlson, 2005), to decrease the frequency and severity of cardiovascular events and mortality (Canner *et al.*, 1986). It exerts its pharmacological effects by (1) inhibiting hepatic diacylglycerol acyltransferase, which results in a decreased triglyceride synthesis and (2) lowering the surface expression of hepatic adenosine triphosphate synthase beta chain, which results in a decreased holoparticle high-density lipoprotein catabolism and increased high-density lipoprotein levels (Gille *et al.*, 2008; Kamanna *et al.*, 2009).

Various cocrystals of NA such as 3,5-dinitrobenzoic acid–nicotinic acid (Ford *et al.*, 2013), 4-aminobenzoic acid–nicotinic acid (Jebas & Balasubramanian, 2006), dipicolinic acid–nicotinic acid (Bankiewicz & Wojtulewski, 2019), gallic acid–nicotinic acid (Kavuru *et al.*, 2010), modafinil–nicotinic acid (Ghosh *et al.*, 2021) and *p*-hydroxybenzoic acid–nicotinic acid (Latha *et al.*, 2020) have been reported. It is, therefore, of great interest to develop new formulations or functional solid state forms of NA through cocrystallization. The present paper describes the electron density analysis of NA cocrystallized with pyrogallol (PY) (Scheme 1, right-hand side) which is a potent component of *Emblica officinalis* (Indian gooseberry) and is found in green tea plants and is used in Asian medicine for its anti-inflammatory and antipyretic properties (Nicolis *et al.*, 2008). The NA–PY cocrystal structure has been reported at 294 (2) K (Prabha *et al.*, 2017).

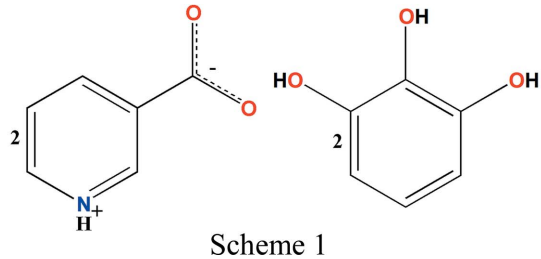

Scheme 1

The experimental distribution of electron density in the cocrystal was modeled from high-resolution X-ray diffraction data using *MoPro* (Guillot *et al.*, 2001; Jelsch *et al.*, 2005) in the Hansen and Coppens (HC) formalism (Hansen & Coppens, 1978). The experimental model is compared with the model obtained from the theoretical structure factors in experimental $\sin\theta/\lambda_{max}$ limits obtained from periodic DFT-D3 single-point energy calculations.

2. Experimental

2.1. Cocrystallization

Nicotinic acid (NA), pyrogallol (PY) and the solvent (ethanol) were sourced from Sigma Aldrich. All chemicals were used without further purification. NA and PY (1:1 molar ratio) were co-ground using pestle and mortar for 30 min. Then they were dissolved in ethanol (10 ml) and the solution was left to crystallize by evaporation at room temperature. Lustrous brown high-quality crystals (Fig. S1) (block morphology) were obtained after 10 days.

2.2. Data collection

2.2.1. X-ray crystallography. A diffraction-quality single crystal (of dimensions 0.24 mm × 0.29 mm × 0.35 mm) was selected under a polarizing microscope and mounted on the tip of goniometer head using vacuum grease (Fig. S1). High-resolution single-crystal X-ray diffraction data were then collected on a Bruker D8 Venture diffractometer equipped with a high-efficiency PHOTON II detector and a micro-focus beam source (monochromatic Mo *Kα* radiation λ = 0.71073 Å). The experiment temperature of 100 (1) K was

Table 1
Experimental details.

Absorption correction: analytical (*SADABS2016/2*; Bruker, 2016) was used for absorption correction. wR_2(int) was 0.0673 before and 0.0563 after correction. The ratio of minimum to maximum transmission is 0.8999.

Crystal data			
Chemical formula	$C_6H_5NO_2{\cdot}C_6H_6O_3$		
M_r	249.22		
Crystal system, space group	Orthorhombic, $Pca2_1$		
Crystal data			
Temperature (K)	100		
a, b, c (Å)	13.6648 (4), 11.9321 (3), 12.9678 (4)		
V (Å^3)	2114.40 (10)		
Z	8		
Radiation type	Mo $K\alpha$		
μ (mm^{-1})	0.12		
Crystal size (mm)	0.35 × 0.29 × 0.24		
Data collection			
Diffractometer	Bruker D8 Venture PHOTON II		
T_{min}, T_{max}	0.675, 0.750		
Refinement (*MoPro*)	IAM	Multipolar	Theoretical
$R[F^2 > 2\sigma(F^2)]$, $wR(F^2)$, S	0.061, 0.059, 1.08 (high order) 0.047, 0.064, 1.08 (all data)	0.034, 0.046, 1.01	0.005, 0.005, 0.09
No. of reflections used	19 169 ($I > 2\sigma$)	19 169 ($I > 2\sigma$)	24319
Weighting scheme	$\sigma w^2 = (a\sigma Y_o^2 + bF_o^2)$ where a = 1.22868, b = 0.00010	$\sigma w^2 = (a\sigma Y_o^2 + bF_o^2)$ where a = 1.22868, b = 0.00010	w = 1.00
No. of parameters	325	1075	707
H-atom treatment	H-atom parameters constrained	H-atom parameters constrained	H atom parameters constrained
$\Delta\rho_{max}$, $\Delta\rho_{min}$ (e Å^{-3})	0.70, −0.51	0.34, −0.34	0.15, −0.12
Absolute structure	Flack x determined using 7550 quotients $[(I^+)-(I^-)]/[(I^+)+(I^-)]$ (Parsons *et al.*, 2013)	8469 Friedel pairs	11836 Friedel pairs
Absolute structure parameter	0.33 (13)	–	–

Computer programs: *SHELXT 2014/5* (Sheldrick, 2014), *SHELXL* (Sheldrick, 2015), *OLEX2* (Dolomanov *et al.*, 2009).

maintained using a stream of dry nitrogen gas using an Oxford Cryosystems COBRA cryostat. The data collection strategy consisted of ω and ϕ scans and the exposure time ranged between 10 to 40 s per frame for low and high angles, respectively, resulting in total 101 259 reflections, merged to 23 980 independent reflections up to of $\sin\theta/\lambda_{max}$ = 1.112 Å^{-1}. The initial cell refinements and data reduction were performed using the program *SAINT* (Bruker, 2016). Indexing of crystal faces and analytical absorption correction were made using the program *SADABS*. The R_{int} value (0.051) of the whole collected diffraction data shows the quality of the data for a reliable charge density analysis. More details related to crystal data, data collection and structural refinement are given in Table 1.

2.3. Structure solution and independent atom model *MoPro* refinement

The cocrystal structure was solved in the orthorhombic polar space group $Pca2_1$ by direct methods using *SHELXT* (Sheldrick, 2014) and the initial independent atom model (IAM) refinement was performed with *SHELXL* (Sheldrick, 2015) and *OLEX2* (Dolomanov *et al.*, 2009). All hydrogen atoms were clearly visible in the difference Fourier maps including those on the N1 and N2 nitrogen atoms of NA, thus confirming the zwitterionic nature of NA moieties. After the *SHELX* refinement, the model was imported to *MoPro* software (Jelsch *et al.*, 2005). In all refinement steps, a $I > 2\sigma(I)$ threshold was used. Initially the scale factor was refined using all the data. Subsequently, a high-order refinement was carried out for proper thermal deconvolution of non-H atoms using reflections with $\sin\theta/\lambda_{max} > 0.8$ Å^{-1}. Table 1 lists the crystallographic and refinement statistics. The bond distances of C—H atoms were initially fixed at neutron positions as obtained from average neutron diffraction values, then to optimized distances from standard DFT calculations (Table S2) as mentioned in the next section. The anisotropic atomic displacement parameters of hydrogen atoms were estimated using SHADE server (Madsen, 2006). Once the high-order refinement converged, only the scale factor was refined using the whole data set. As NA–PY crystallizes in a polar space group (El-Haouzi *et al.*, 1996), deformation electron density maps (Figs. 1 and S3) were generated to estimate the possibility of a thorough charge density analysis. The minimum and maximum electron density peaks observed in Fourier maps are −0.51 and 0.71 e Å^{-3}, respectively (Fig. 1). These deformation maps prior to multipolar refinement reveal a well distributed electron density on covalent bonds and lone pairs despite the noncentrosymmetry of the crystal (space group $Pca2_1$) (Souhassou *et al.*, 1991).

2.4. Multipolar refinement

The multipolar atom model refinement was carried on the basis of HC (Hansen & Coppens, 1978) multipolar formalism with *MoPro* (Jelsch *et al.*, 2005). In the initial stages of

refinement, chemical constraints were imposed between chemically equivalent atoms as given in Tables S1*A*–S1*C*. The data and model quality were checked by normal probability plot (Zhurov *et al.*, 2008) and fractal dimension plot (Figs. S2*A* and S2*B*). During the multipolar refinement P_{val}, κ, P_{lm} and κ' were refined in a step-by-step manner together with the scale factor; subsequently all charge density parameters were refined and along with the position and thermal displacement parameters. H atom's κ and κ' were restrained to 1.16 (2). All heavy atoms were refined to octapolar level while the H atoms were refined to dipolar level. However, at the end of this refinement, the valence populations on COO^- oxygen atoms were surprisingly found to be positive. Various strategies were tried, including the lifting of the constraints, but the valence populations did not improve. One of the reasons for this failure could be that the space group ($Pca2_1$) is polar. El Haouzi and Hansen have shown that free refinement of odd-order multipoles in polar space groups leads to meaningless results due to a large change of phases, therefore, it is necessary to apply constraints (El Haouzi *et al.*, 1996). Even if our problem concerns P_{val} parameters, to circumvent this problem, the refinement was started using the transferable multipolar data base ELMAM2 (Pichon-Pesme *et al.*, 1995; Domagała *et al.*, 2012). After the transfer, initially only the position and thermal displacement parameters were refined. Subsequently, multipolar parameters were refined and then P_{val} and kappas parameters. When converged all charge density parameters along with position and thermal motion were fitted. The chemical constraints on oxygen atoms were gradually lifted. This strategy was successful as valence population after this ELMAM2 strategy stayed negative as expected. The minimum and maximum electron density peaks

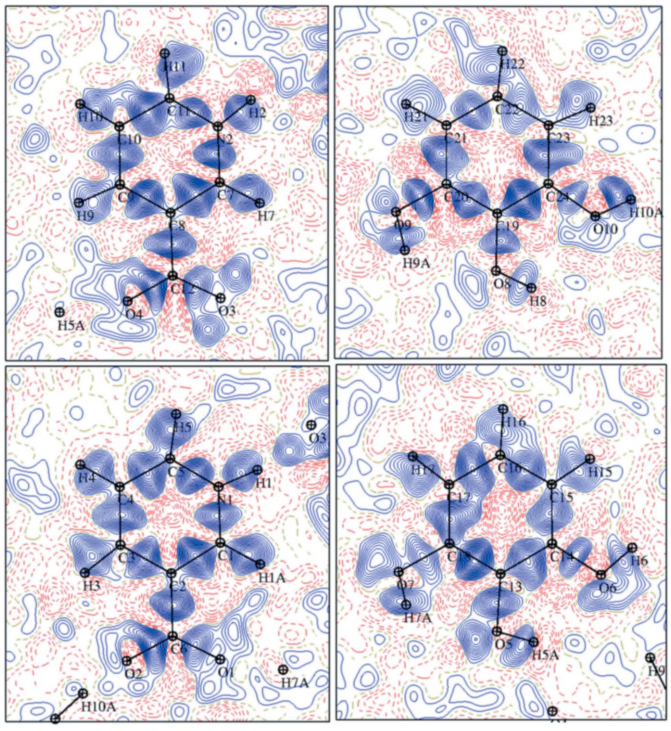

Figure 1
Deformation electron density maps of NA moieties (left) and PY moieties (right), after IAM refinement with *MoPro* at 0.05 e Å^{-3} level with $\sin\theta/\lambda_{max}$ = 0.8 Å^{-1}.

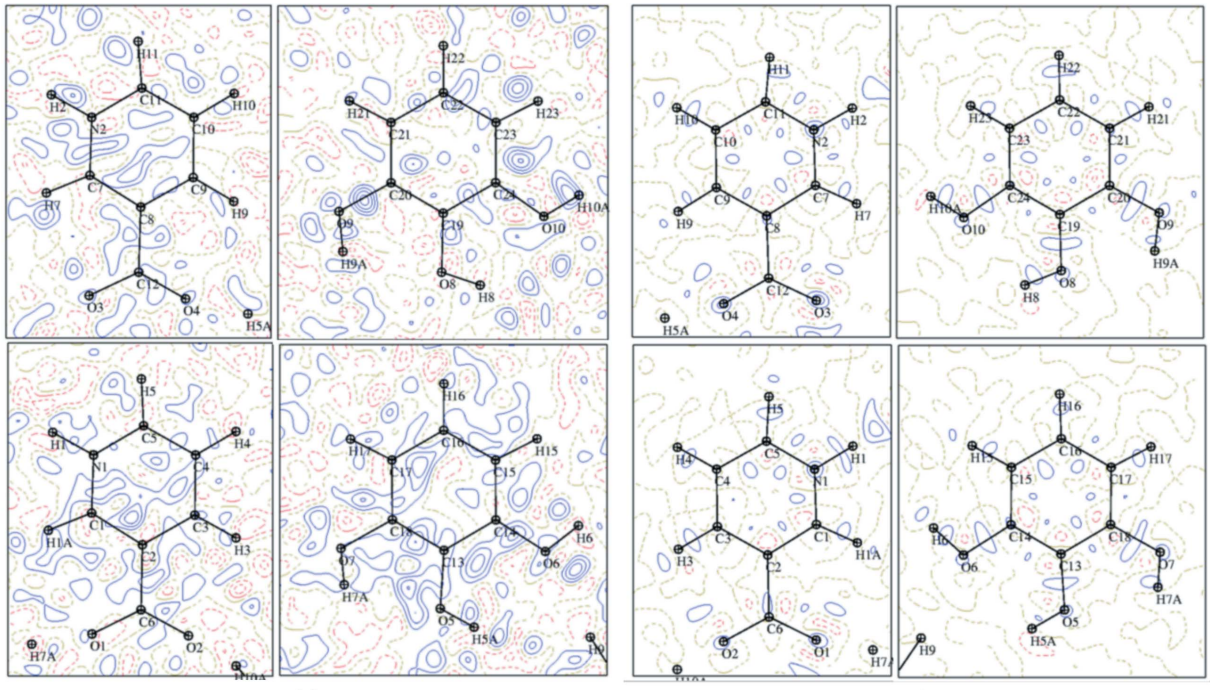

(*a*) (*b*)

Figure 2
(*a*) Residual electron density maps of NA moiety (left) and PY moiety (right), after MM_{exp} with *MoPro* at 0.05 e Å^{-3} contour level with $\sin\theta/\lambda_{max}$ = 0.8 Å^{-1} and $I > 2\sigma(I)$. (*b*). Residual electron density maps of NA moiety (left) and PY moiety (right), after MM_{theo} with *MoPro* at 0.05 e Å^{-3} contour level with $\sin\theta/\lambda_{max}$ = 0.8 Å^{-1}.

observed in residual density maps are −0.34 and 0.34 e Å^{-3}, respectively, see Figs. 2(*a*) and S4 (all data). The residual density maps are clean as compared to IAM maps even if some electron density remains on bonds.

2.5. Theoretical calculations

Two types of DFT calculations were carried out. A preliminary periodic DFT partial geometry optimization was performed starting with the unit cell and atomic positions obtained from the *MoPro* IAM refinement where the hydrogen atoms were fixed to the standard neutron distances. All non-hydrogen atoms in the unit cell were fixed and only hydrogen atoms were allowed to relax during the optimization with fixed unit-cell parameters using the *pw.x* module of the *Quantum-Espresso* (Giannozzi *et al.*, 2017) package. Ultrasoft pseudopotentials were used for all atoms using the Perde–Burke–Ernzerhof (PBE) (Perdew *et al.*, 1996) exchange–correlation approximation in combination with Grimme's D3 correction for dispersion interactions (Grimme *et al.*, 2010). The atomic coordinates of hydrogen atoms were relaxed using the damped (quick-min Verlet) dynamics for structural relaxation until the forces exerted on the atoms were less than 10^{-4} (a.u.) with 10^{-7} (a.u.) convergence threshold on total energy. The cutoff energy and electronic density of plane-waves was set to be 60 Ry and 625 Ry, respectively. The mesh of the unit cell for *k*-point sampling was 2 × 3 × 2 which corresponds to ∼0.2 Å^{-1} of *k*-space resolution. The obtained hydrogen distances were used to complete *MoPro* IAM and MM_{exp} (MM = multipolar model) refinements.

Following multipolar refinement of the experimental model described above using the optimized hydrogen distances, another periodic DFT-D3 single-point energy calculation was performed using the all-electron frozen-core projector-augmented wave (PAW) (Blöchl, 1994) approach instead of pseudopotentials. Experimental unit-cell parameters and atomic coordinates obtained from the MM_{exp} were used as input for the *Quantum-Espresso* single-point energy calculation. The standard PBE PAW atomic data sets were used to describe the wavefunction and the density in the augmentation spheres. Partial occupancies were calculated using Fermi–Dirac smearing. The electron density was represented on a dense real-space grid comprising 360 × 360 × 360 points along the crystallographic axes. The mesh of the unit cell for *k*-point sampling was enhanced to 5 × 5 × 5 which corresponds to a resolution of ∼0.1 Å^{-1}. The cutoff energy and electronic density of plane-waves was set high at 75 Ry and 840 Ry, respectively, to ensure convergence and accuracy. The all-electron charge density (valence and core) was obtained in cube file format using *pp.x* package of *Quantum-Espresso*. The Fourier transform of electron density was performed to obtain static theoretical structure factors up to the experimental $\sin\theta/\lambda$ limits using a python script developed by one of us (AM) and is available on request via email. The multipole refinement was performed using *MoPro* on the charge density reconstructed from these theoretical structure factors and results are represented here as MM_{theo}. During the MM refinement using theoretical structure factors, the thermal parameters of atoms were set to zero and only scale factor and charge density parameters were refined whereas the atomic positions were fixed at MM_{exp} level. Only scale factor, kappas,

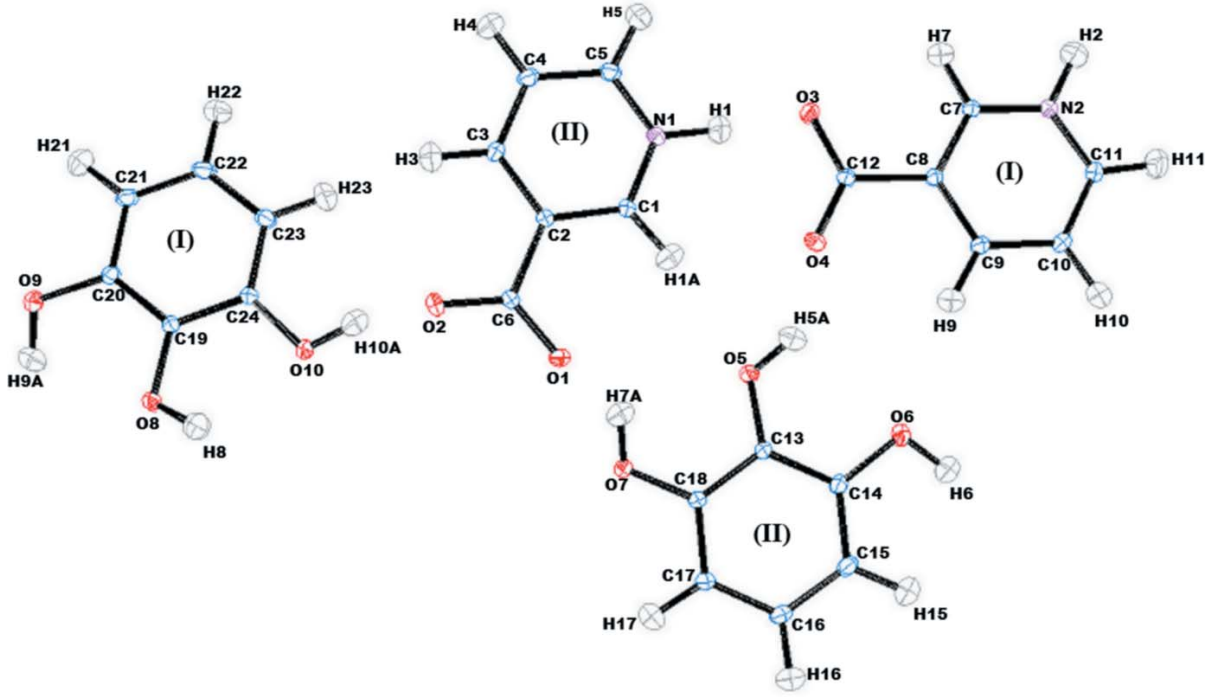

Figure 3
A thermal ellipsoid plot of the asymmetric unit of NA–PY cocrystal showing the atom numbering scheme for non-hydrogen atoms; ellipsoids are drawn at 50% probability level.

multipoles and valence population were refined by keeping the weighting scheme equal to 1. The residual electron density maps after theoretical multipolar refinement are given in Fig. 2(*b*).

3. Results and discussion

3.1. Crystal structure analysis: zwitterion nature of NA

The room-temperature crystal structure of NAPY has been reported previously using cocrystals obtained by a slow evaporation method (Prabha *et al.*, 2017). In the present study, we prepared the same cocrystals by a dry grinding method and got better quality, highly diffracting crystals. We have re-determined the structure of the cocrystal at 100 K to explore the charge density features. NA–PY crystallizes in the non-centrosymmetric polar space group ($Pca2_1$). The structure of the asymmetric unit after multipolar refinement is shown in Fig. 3. Further details of bond lengths and bond angles after IAM and multipolar atom model (MAM) are given in the supporting information.

NA exists in two tautomeric forms: as neutral and zwitterion ions (Kutoglu & Scheringer, 1983; Takusagawa & Shimada, 1976). In NA–PY, NA exists as a zwitterion. The asymmetric unit contains zwitterionic NA molecules and PY molecules in a ratio of 2:2. In the NA (I) moiety, the C—O bond distances are 1.2693 (5) Å and 1.2483 (5) Å for C12—O3 and C12—O4, respectively, while the corresponding values in NA (I) moiety are 1.2511 (5) Å and 1.2674 (5) Å in NA (II) for C6—O2 and C6—O1, respectively. This confirms the zwitterion nature of NA and shows resonance of COO^- group. The charge separation or zwitterion formation is due to strong solvation (Khan *et al.*, 1977; Medvedev *et al.*, 2013; Nagy & Takács-Novák, 1997). The PY molecules are able to form a cocrystal using their COOH groups by transforming the COOH···N (pyridine ring) heterosynthon into a $COO^-\cdots{}^+N$—H heterosynthon, thus forming robust charge-assisted non-covalent interactions. Cocrystals or complexes containing zwitterion NA moieties have already reported (Bankiewicz & Wojtulewski, 2019; Kavuru *et al.*, 2010; Athimoolam & Natarajan, 2007).

The geometrical analysis of crystal structure and molecular packing shows a strong network of non-covalent interactions. The formation and stabilization of the NA–PY cocrystal is anchored by four hydrogen bonds (N1—H1···O3, O5—H5*A*···O4, O10—H10*A*···O2 and O7—H7*A*···O1) and other weak interactions due to three functional groups (NH, carboxyl and hydroxyl groups). Ranking these strong interactions cannot be done only on geometrical criteria; this will be discussed later on the basis of the topological analysis of the electron density. All heteroatoms of both NA molecules and PY molecules are involved in the formation of various strong to weak hydrogen bonds on the basis of classification of hydrogen bonding (Koch *et al.*, 1995) (Table S3). The O7 of PY (II) and O8, O9, O10 of PY (I) serve as both hydrogen-bond donor and acceptor to form hydrogen bonds such as O9—H9*A*···O7^{vii}($-x+1, -y+2, z-\frac{1}{2}$), O6—H6···O9^{ii}($x, y-1, z+1$), O9—H9*A*···O8, O8—H8···O10, O5—H5*A*···O4, O8—H8···O3^{iii}($x, y+1, z$), O10—H10*A*···O2 and O7—H7*A*···O1. Along the *a* axis, PY molecules are arranged in a zigzag pattern forming an homosynthon through interlinked O—H···O hydrogen bonds but they are weaker than in the NA homosynthon. NA and PY molecules are linked via O—H···O and N—H···O hydrogen bonds. Along the *b* axis in the unit cell, the NA and PY molecules are interlinked by forming a heterosynthon resulting in O—H···O and N—H···O hydrogen bonds forming a standard brickwall arrangement. Along the *c* axis, PY and NA molecules are arranged in

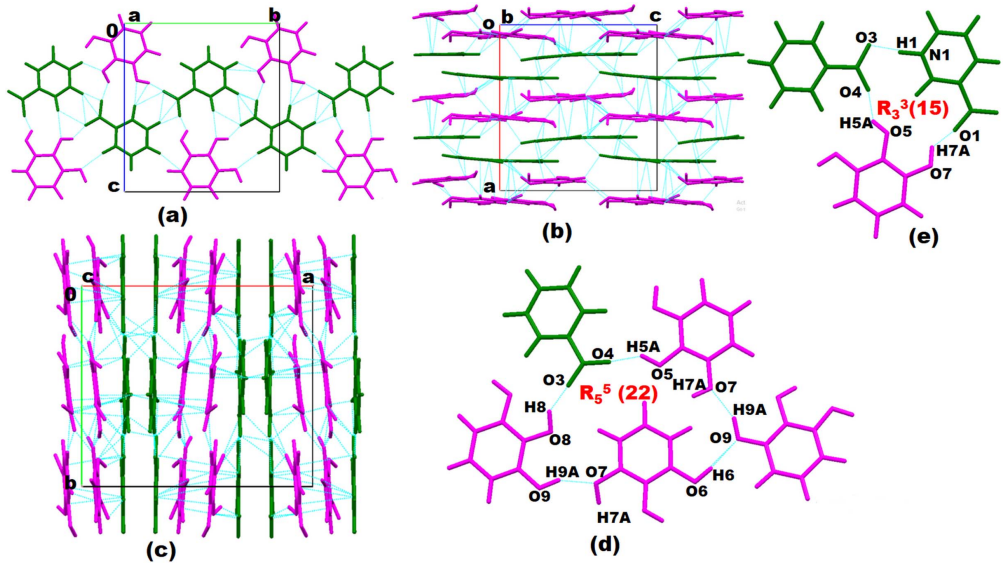

Figure 4
A view of the packing arrangement of the cocrystal of NA (green) with pyrogallol (purple). (*a*) Zigzag pattern of NA and PY along the *a* axis. (*b*) Brick-wall pattern (also called *β*-sheet) along the *b* axis. (*c*) Formation of parallel layers along the *c* axis. (*d*) and (*e*) are ring motifs. The blue lines are hydrogen bonds.

parallel layers forming both a homosynthon and a heterosynthon resulting in N—H···O and O—H···O hydrogen bonds (Fig. 4).

3.2. Electron density analysis

3.2.1. NA and PY molecules. The 2D and 3D static deformation electron density maps of NA and PY based on experimental and theoretical models have been given in Figs. 5, S5 and S6, which show the accumulation of electron density in covalently bonded regions, the position of lone pairs of heteroatoms and the shape of bonded regions. Both experimental and theoretical maps are in agreement. All bond peaks are in line with the published data. The lone pairs on carbonyl oxygen atoms (O3, O4, O1 and O2) are bifurcated and there is tetrahedral symmetry of hydroxyl-oxygen lone pairs (O5, O6, O7 O8, O9 and O10) as shown in Fig. S7. A strong directional character of the hydrogen bonds has been observed. For example, it is observed that the H1 atom arrives in the direction of the lobes of the lone pairs of O3 (Fig. 6). There is strong polarization of electron density in the C—O bond in the COO^{-} group of NA (I) and NA (II) molecules. These findings are also supported by the deformation densities obtained from MM_{theo} (Fig. S5). To further analyze the electron density distribution, we performed the topological study of electron density using the parameters obtained from both of experimental and theoretical refinement models.

The covalent bond analysis was done by using 'Atoms in Molecules' (AIM) theory (Bader, 1990). Fig. S11 shows the real space plots of the positions of critical points and the associated topological properties are listed in Table S4. The position of critical points (CP) of homonuclear (C—C) bonds are in middle of the bond while heteronuclear (N—H, O—C, H—C and C—N) CPs are closer to the electropositive atom than to the electronegative atom, both for experimentally and theoretically calculated covalent bond critical points. From the position of the bond critical point, it is confirmed that O—H, N—H and C—N bonds are polarized and, not surprisingly, the C—C, C—H and C—C bonds are non-polar. The electron densities of H1 and H2 atoms are remarkably delocalized towards their acceptor atoms as evident from the 2D Laplacian maps in Fig. S8 calculated after MM_{exp} while Fig. S9 shows the 3D Laplacian map. Fig. S10 shows the Laplacian

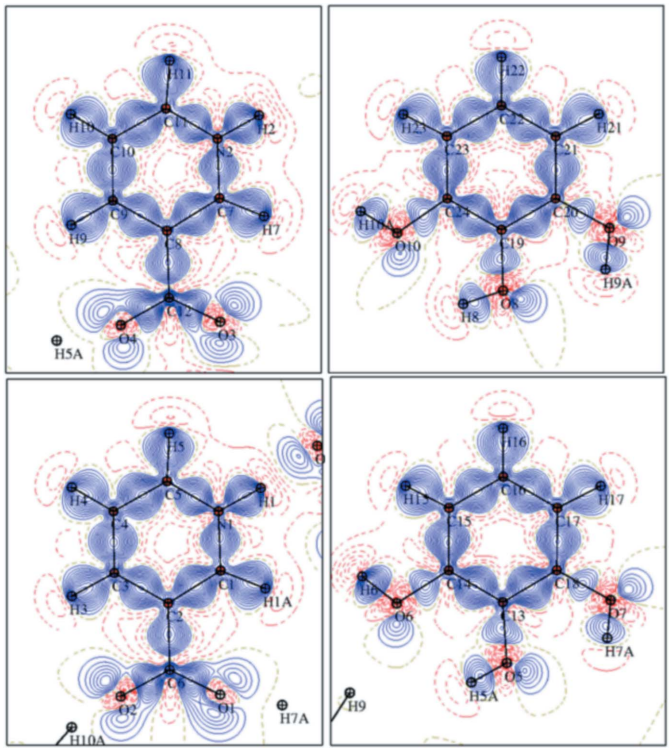

Figure 5
Static deformation electron density distribution of NA (right) and PY (left) after MM_{exp} at 0.05 e $Å^{-3}$ contour level.

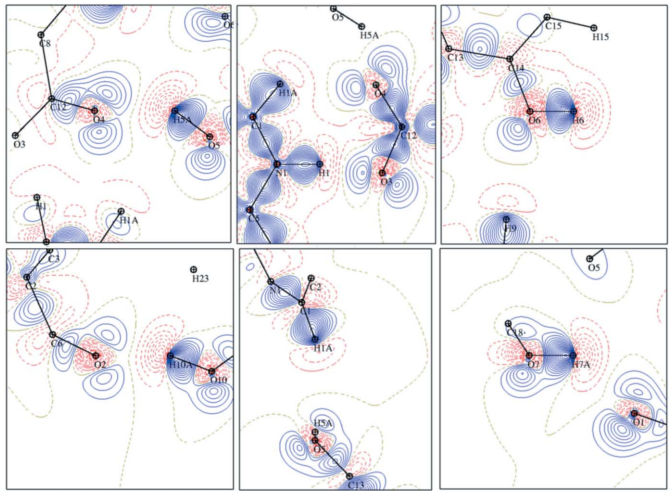

Figure 6
The directionality of the hydrogen-donor atom of the hydrogen bond pointing towards lone pairs of oxygen-acceptor atom of carboxyl group of NA and hydroxyl group of PY.

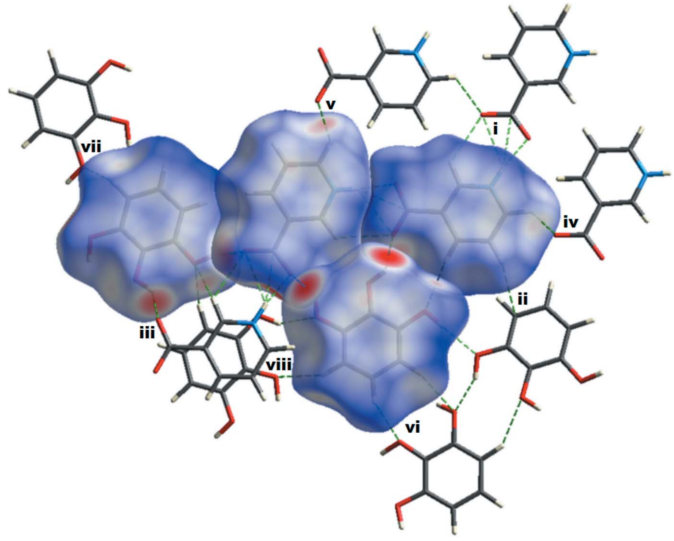

Figure 7
Hirshfeld surface showing interactions of the cocrystal with other neighboring molecule. Symmetry codes: (i) $x, y-1, z$; (ii) $x, y-1, z+1$; (iii) $x, y+1, z$; (iv) $-x+\frac{3}{2}, y-1, z+\frac{1}{2}$; (v) $-x+\frac{3}{2}, y, z-\frac{1}{2}$; (vi) $-x+1, -y+1, z+\frac{1}{2}$; (vii) $-x+1, -y+2, z-\frac{1}{2}$; (viii) $-x+1, -y+2, z+\frac{1}{2}$.

Table 2
Topological values of the interactions (exp/theo).

Distance values (Å), electron density (e Å^{-3}), Laplacian (e Å^{-5}), G_{cp} = bond kinetic energy density (kJ mol^{-1}), V_{cp} = bond potential energy (kJ mol^{-1}). The upper line in each pair is experimental value and lower lines are the theoretical values obtained after multipolar refinement using theoretical structure factors from periodic DFT-D3 single-point energy calculations.

No.	Interactions	Interacting species	d_{12}	d_{1cp}	d_{2cp}	$\rho_{cp(r)}$	$\nabla^2_{\rho(cp)}$	G_{cp}	V_{cp}
1	N1—H1···O3	NA (II) ···NA (I)	1.593	0.502	1.092	0.436 (3)	0.624	89.770	−162.530
			1.590	0.521	1.070	0.401 (3)	0.955	139.910	−172.090
2	N2—H2···O1^{i}	NA (I) ···NA (II)	1.653	0.530	1.124	0.398 (3)	0.661	79.30	−140.60
			1.652	0.547	1.106	0.328 (3)	3.943	120.34	−133.30
3	O10—H10*A*···O2	PY (I) ···NA (II)	1.678	1.158	0.520	0.233 (3)	2.940	81.010	−81.930
			1.691	1.132	0.572	0.228 (3)	3.946	98.240	−89.020
4	O5—H5*A*···O4	PY (II) ···NA (I)	1.825	1.221	0.604	0.174 (3)	2.432	61.050	−55.870
			1.821	1.171	0.661	0.204 (3)	2.929	75.240	−70.710
5	O9—H9*A*···O7^{vii}	PY (I) ···PY (II)	1.902	0.622	1.282	0.155 (3)	1.535	41.82	−41.83
			1.911	0.705	1.215	0.167 (3)	2.462	60.50	−53.92
6	O7—H7*A*···O1	PY (II) ···NA (II)	1.899	1.242	0.658	0.149 (3)	2.322	55.300	−47.350
			1.890	1.191	0.707	0.191 (3)	2.536	65.880	−62.680
7	O8—H8···O3^{iii}	PY (I) ···NA (I)	1.930	0.669	1.262	0.137 (3)	2.064	48.82	−41.44
			1.913	0.716	1.220	0.151 (3)	2.448	57.89	−49.09
8	O6—H6···O9^{ii}	PY (II) ···PY (I)	1.994	0.668	1.327	0.131 (3)	0.882	26.55	−29.09
			1.991	0.713	1.279	0.115 (3)	2.059	45.83	−35.59
9	C5—H5···O8^{v}	NA (II) ···PY (I)	2.337	0.982	1.388	0.073 (2)	1.273	27.07	−19.47
			2.348	0.996	1.371	0.078 (2)	1.192	26.12	−19.78
10	C21—H21···O10^{vii}	PY (I) ···PY (I)	2.342	0.928	1.416	0.071 (2)	1.078	23.35	−17.34
			2.366	0.976	1.406	0.063 (2)	1.018	21.59	−15.46
11	C7—H7···O10^{i}	NA (I) ···PY (I)	2.359	0.925	1.439	0.064 (2)	0.860	18.80	−14.17
			2.355	0.949	1.426	0.056 (2)	1.035	21.39	−14.57
12	C16—H16···O5^{vi}	PY (II) ···PY (II)	2.445	1.015	1.445	0.060 (2)	0.947	20.05	−14.32
			2.424	1.038	1.418	0.057 (2)	0.955	19.96	−13.90
13	C1—H1*A*···O4	NA (II) ···NA (II)	2.432	0.953	1.481	0.053 (2)	0.971	19.990	−13.530
			2.468	1.045	1.434	0.059 (2)	0.910	19.350	−13.920
14	C11—H11···O2^{iv}	NA (I) ···NA (II)	2.512	1.101	1.456	0.052 (2)	0.908	18.73	−12.73
			2.519	1.114	1.421	0.061 (2)	0.879	18.90	−13.88
15	C5—H5···O8^{i}	NA (II) ···PY (I)	2.547	1.130	1.475	0.051 (2)	0.896	18.45	−12.49
			2.536	1.121	1.442	0.056 (2)	0.862	18.22	−12.96
16	C9— H9···O6	NA (I) ···PY (II)	2.512	1.501	1.012	0.046 (2)	0.673	14.050	−9.770
			2.521	1.484	1.046	0.041 (2)	0.674	13.780	−9.210
17	C7—H7···O2^{i}	NA (I) ···NA (II)	2.506	0.988	1.520	0.045 (2)	0.828	16.84	−11.13
			2.538	1.094	1.474	0.047 (2)	0.787	16.24	−11.03
18	C15—H15···O9^{ii}	PY (II) ···PY (I)	2.547	1.054	1.494	0.043 (2)	0.689	14.15	−9.54
			2.567	1.086	1.496	0.047 (2)	0.740	15.32	−10.49
19	C17—H17···O8^{viii}	PY (II) ···PY (I)	2.525	1.029	1.497	0.043 (2)	0.676	13.94	−9.47
			2.560	1.099	1.533	0.027 (2)	0.624	12.10	−7.19
20	C15—H15···O7^{vi}	PY (II) ···PY (II)	2.634	1.114	1.546	0.041 (2)	0.649	13.33	−8.98
			2.605	1.127	1.547	0.045 (2)	0.675	14.02	−9.64
21	C11—H11···O7	NA (I)···PY (II)	2.728	1.216	1.569	0.035 (2)	0.629	12.60	−8.09
			2.719	1.208	1.521	0.042 (2)	0.623	12.92	−8.88
22	C1—H1*A*···O5	NA (II) ···PY (II)	2.691	1.102	1.605	0.034 (2)	0.369	7.790	−5.540
			2.703	1.125	1.585	0.031 (2)	0.470	9.490	−6.190
23	C23—H23···O5	PY (I) ···PY (II)	2.895	1.249	1.672	0.024 (2)	0.375	7.43	−4.66
			2.882	1.287	1.655	0.027 (2)	0.390	7.85	−5.09
24	C4—H4···O1	NA (II)···NA (II)	2.887	1.256	1.644	0.022 (2)	0.376	7.38	−4.53
			2.897	1.297	1.623	0.024 (2)	0.378	7.46	−4.64
25	C9—H9···O3	NA (I) ···NA (I)	3.186	1.517	1.742	0.014 (2)	0.219	4.22	−2.48
			3.200	1.493	1.735	0.014 (2)	0.214	4.15	−2.47
26	C10—H10···O3	NA (I)···NA (I)	3.195	1.482	1.764	0.014 (2)	0.230	4.44	−2.62
			3.177	1.465	1.731	0.014 (2)	0.220	4.27	−2.54

Symmetry codes: (i) $x, y-1, z$; (ii) $x, y-1, z+1$; (iii) $x, y+1, z$; (iv) $-x+\frac{3}{2}, y-1, z+\frac{1}{2}$; (v) $-x+\frac{3}{2}, y, z-\frac{1}{2}$; (vi) $-x+1, -y+1, z+\frac{1}{2}$; (vii) $-x+1, -y+2, z-\frac{1}{2}$; (viii) $-x+1, -y+2, z+\frac{1}{2}$

maps of NA and PY after MM_{theo}. All the topological parameters of the covalent bonds are consistent with the literature.

3.3. Hirshfeld surface map and fingerprint plot analyses

In order to explore various types of intermolecular interaction sites and for quantitative distribution of intermolecular interactions involved in crystal packing, Hirshfeld surface analysis (Spackman & Byrom, 1997; McKinnon *et al.*, 2004; Spackman & Jayatilaka, 2009) was performed. The Hirshfeld surface maps and fingerprint plots of the cocrystal of NA–PY, mapped with normalized contact distance d_{norm}, were generated by *Crystal Explorer* (Turner *et al.*, 2017) and show the N—H···O and O—H···O interactions with neighboring molecules. The dark-red spots in Fig. 7 represent the strong

hydrogen bonding, blue spots represent the longer contacts and white areas show the contacts which are closer to van der Waals radii and colors express the chemical environment of the cocrystal molecule. The Hirshfeld surface map confirms what was already discussed on the basis of O···H distances, showing the strong hydrogen bonds (N2—H2···O1^{i}, N2—H2···O2^{i}, O6—H6···O9^{ii}, O8—H8···O3^{iii}) as well as weak interactions (C7—H7···O2^{i}, C5—H5···O4^{v}, C16—H16···O5^{vi}, C21—H21···O10^{vii}, C17—H17···O8^{viii}) in the vicinity of O1, O2, O3, O4, O5 and O8 atoms of the cocrystal of NA–PY; the strength of these intermolecular interactions must be quantified using the topological analysis of electron density in particular intermolecular critical points given in Table 2.

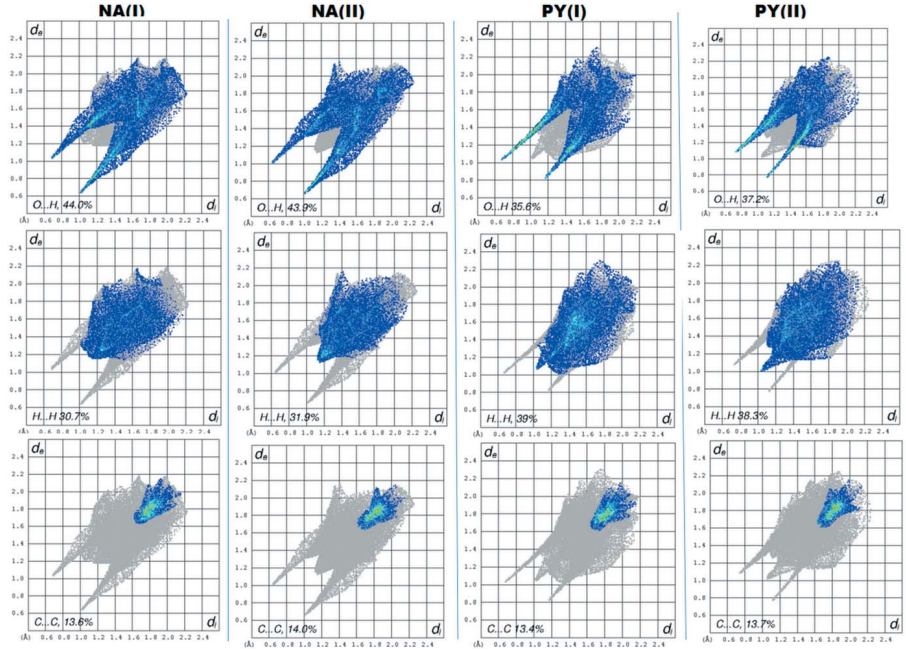

Figure 8
Fingerprint plots of NA (I), NA (II), PY (I) and PY (II) showing the percentage of interactions of O···H/H···O, H···H and C···C in cocrystal of NA–PY.

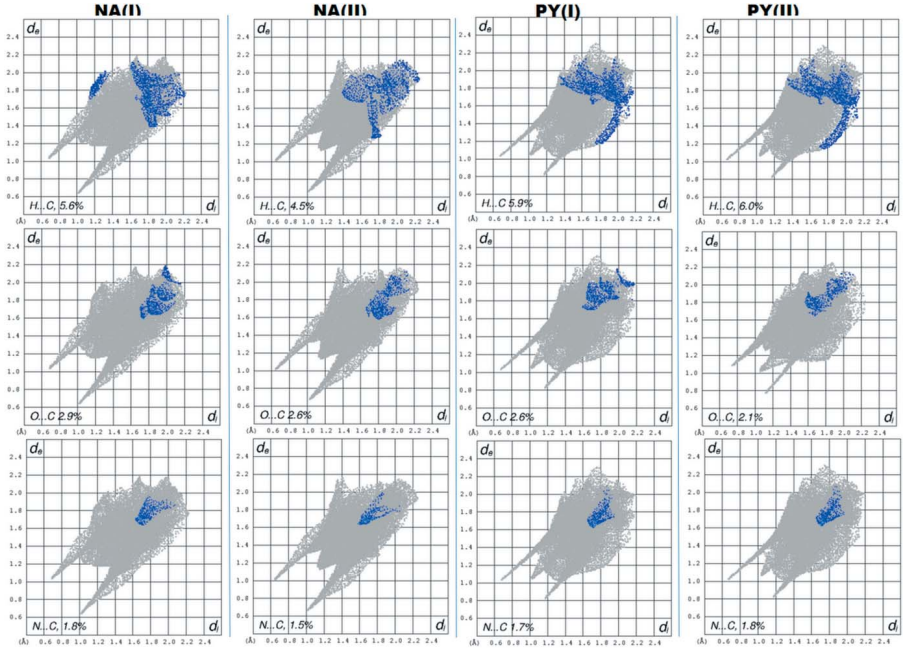

Figure 9
Fingerprint plots of NA (I), NA (II), PY (I) and PY (II) showing the percentage of interactions of H···C/C···H, O···C/C···O and N···C/N···C in the cocrystal of NA–PY.

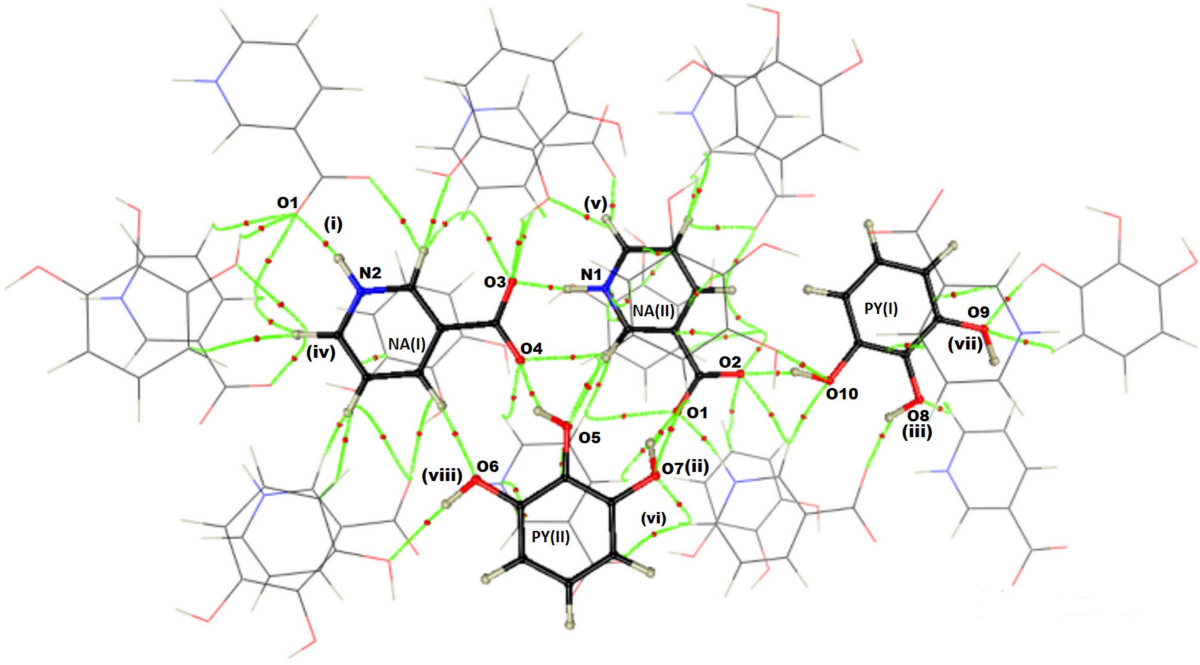

Figure 10
A view of the molecular cluster showing the interaction lines (green) and the critical points (brown). Residues in bold show the asymmetric unit. Symmetry codes: (i) x, $y-1$, z; (ii) x, $y-1$, $z+1$; (iii) x, $y+1$, z; (iv) $-x+\frac{3}{2}$, $y-1$, $z+\frac{1}{2}$; (v) $-x+\frac{3}{2}$, y, $z-\frac{1}{2}$; (vi) $-x+1$, $-y+1$, $z+\frac{1}{2}$; (vii) $-x+1$, $-y+2$, $z-\frac{1}{2}$; (viii) $-x+1$, $-y+2$, $z+\frac{1}{2}$.

Fingerprint plots are very useful and are a unique way to find out the percentage of interactions of strong hydrogen bonding, close contacts and other types of interactions. Fingerprint plots gives us a brief summary of the frequency of each combination of d_e and d_i (distance from a point on the surface to the nearest nucleus outside the surface is represented by d_e while distance from a point on the surface to the nearest nucleus inside the surface is represented by d_i) across the surface of the molecule derived from the Hirshfeld surface. The fingerprint plots of the cocrystal of NA–PY in Fig. 8 show two sharp spikes in two NA and two PY plots which correspond to interactions sites of O···H/H···O 44.0% and 43.9% in NA (I) and NA (II), respectively, and 35.6% and 37.2% in PY (I) and PY (II), respectively. The H···H interactions are indicated by broader areas between the spikes are 30.7% in NA (I) and 31.9% in NA (II) and by the elongated region between the spikes are 39.0% in PY (I) and 38.3% in PY (II) and have a great participation in cocrystal structure relative to other interactions. The π–π interactions are represented by diffused green spots in fingerprint plots and contribute about 13.6% and 14.0% in NA (I) and NA (II), respectively, and 13.4% and 13.7% in PY (I) and PY (II), respectively, and results in π–π stacking. Many other types of interactions are also found in NA (I), NA (II), PY (I) and PY (II) in very low percentages as shown in Fig. 9.

3.4. Topological analysis of intermolecular interactions

A topological analysis of electron density of intermolecular bond critical points was performed for all interactions involved in the crystal packing under the realm of AIM (Bader, 1990). All the N—H···O, O—H···O and C—H···O type interactions fulfill the first four of Koch and Popelier's criteria (KP; Koch & Popelier, 1995; Popelier, 2000) and hence can be classified as hydrogen bonds. All the interactions have positive values of Laplacian at bond critical points, confirming closed shell interactions. Table 2 lists the topological parameters of (3, −1) bond critical points (BCPs) for the main interactions; they have been arranged based on the decreasing value of electron density at the bond critical points (ρ_{cp}). There is a close agreement between experimental and theoretical values of all the topological parameters which shows

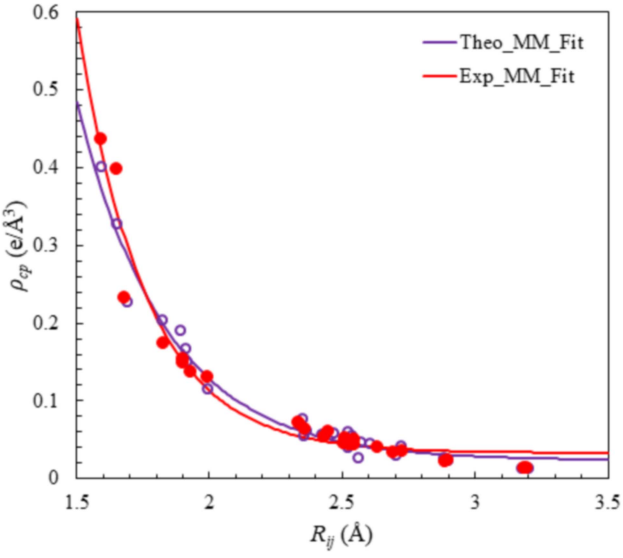

Figure 11
Exponential dependence of ρ_{cp} (e Å^{-3}) on the bond path length R_{ij} (Å) using 26 data points.

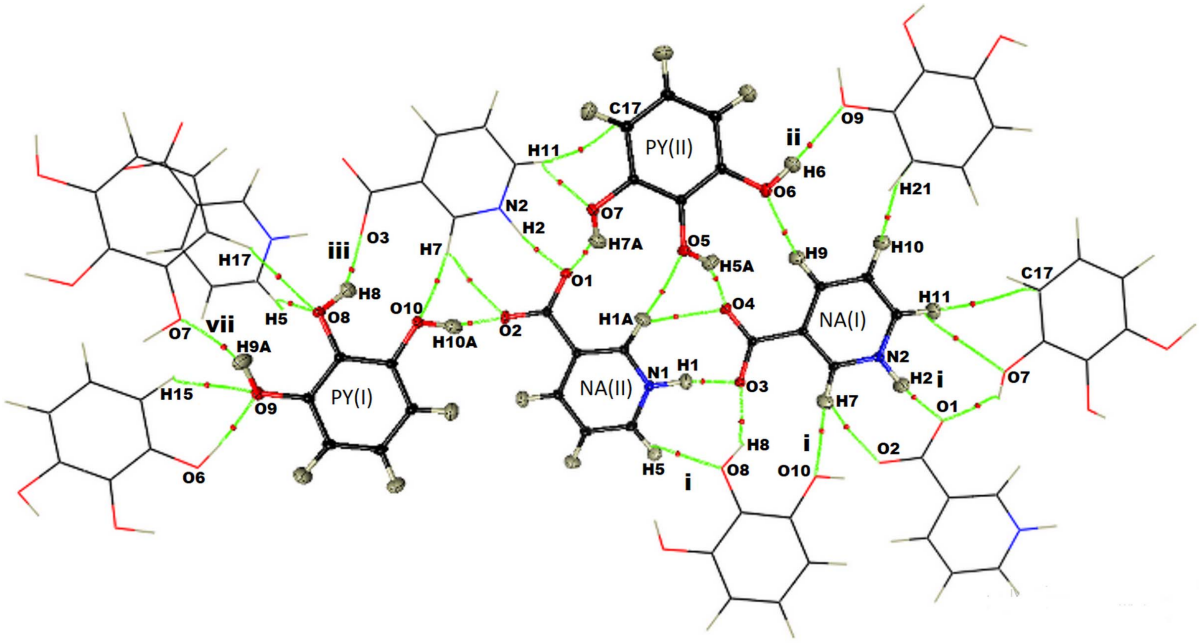

Figure 12
A view of the polymeric chain extending along one dimension, showing the interaction lines (green) and the critical points (brown) for strong hydrogen bonds. Residues in bold show the asymmetric unit. Symmetry codes are same as in Fig. 10.

the accuracy of the models. As shown in Table 2 and Fig. 10 the strongest interactions are between the NA zwitterions, followed by strong to moderate NA–PY hydrogen bonds, the weakest interactions being between the PY molecules. The exponential dependence of ρ_{CP} on R_{ij} of all these hydrogen bonds is in agreement with the literature (Espinosa *et al.*, 1998, 1999; Mallinson *et al.*, 2003; Munshi & Guru Row, 2005; Dominiak *et al.*, 2006; Mata *et al.*, 2010). The coefficients of determination R^2 obtained between ρ_{CP} and R_{ij} is 0.096 (Fig. 11). This topological analysis provides insight into the mechanism of nucleation and growth of the cocrystal. Based on the electron density at BCP, the strongest hydrogen bonds are the two N—H···O-types connecting the zwitterionic nicotinic acid into a polymeric chain which extends along one-dimension (Fig. 12). Both NA (I)···NA (II) hydrogen bonds have remarkably short H···acceptor distances (1.59 and 1.65 Å, respectively). Only one of the two carboxylate oxygen atoms of NA (I) and NA (II) (O3 and O1) form these strong hydrogen bonds. The ionic covalent nature of the bonds is confirmed by the very high values of ρ at the respective BCPs ($\simeq$ 0.4 e Å^{-3}) for both of them. In addition, the values of kinetic (G_{cp}) and potential energy densities (V_{cp}) are also very large. The potential energy density for the NA–NA interactions is much larger than the kinetic one which substantiate the argument that these interactions have an important covalent character. This features may explain why $Z' = 2$. These interactions are the foundation stone of this cocrystal system responsible for the onsets of the process of nucleation linking the NA molecules into a chain defining the NA substructure. The next significant hydrogen bonds in the hierarchy are O10—H10*A*···O2 and O5—H5*A*···O4 with short distances and quite an elevated ρ value at the BCP (0.23 e Å^3) connecting NA (II) to PY (I) and NA (I) to PY (II) moiety via O2 and O4 atoms which are not strongly involved in the NA substructure. PY (I) also connects with the next NA (I) moiety through O8—H8···O3 ($\rho \simeq 0.14$ e Å^{-3}). It further connects with PY (II) units through O9 atom via H9*A*···O7 and by accepting H6—O6. The topological parameters of both PY–PY hydrogen bonds are similar to each other. They have almost equal values of electron density at the BCPs ($\rho \simeq 0.15$ e Å^3) and values of kinetic (G_{cp}) and bond potential energy (V_{cp}) are also similar. The O1 atom of NA (II) forms a bifurcated hydrogen bond with a PY (II) moiety (O7—H7*A*···O1) and an NA (I) moiety (N2—H2···O1) to form a trimer and thus resulting in 'solvation' of the NA chain which is possibly the initiation of the cocrystallization process. In conclusion, on the basis of the topological analysis, in particular ρ (CP) the strength of the driving interactions can thus be ranked as NA–NA > NA–PY > PY–PY. Such a hierarchy of hydrogen bonds would not have been found solely based on hydrogen bond distances.

In addition to these classical hydrogen bonds, there are 18 C—H···O interactions which have reasonable values of electron density at the critical points (ranging from 0.073 to 0.014 e Å^{-3}); they are characterized by positive Laplacian values confirming their closed shell nature. Among them, C5—H5···O8^{v} [2.337 Å; (v) $-x+\frac{3}{2}, y, z-\frac{1}{2}$] is the strongest interaction; electron density is 0.073/0.078 e Å^{-3} and Laplacian of electron density is 1.273/1.192 e Å^{-5}. Therefore a strong NA–NA substructure initializes the crystallization and the PY molecules fill the cavities of this substructure.

4. Conclusions

We have successfully synthesized the cocrystal of nicotinic acid and pyrogallol (NA–PY) and obtained high-resolution X-ray data which allowed us to perform accurate charge density analysis to calculate the electron-density-derived properties. The experimental results are in agreement with high-level DFT calculations in the solid state. Whereas the availability of high-resolution data is necessary condition to perform a charge density analysis, centrosymmetry of the crystal system is also a desired goal as it makes solution of the phase problem quite simple. The absence of the latter particularly for polar space groups can arouse certain challenges in the precise modeling of the electron density parameters. A rigorous refinement strategy may be needed to arrive at an acceptable solution, for example, by initially setting the electron density parameters to standard values from an electron density database.

The strong electrostatic forces of attraction between zwitterions are involved to first build a crystal substructure which later on stabilizes the cocrystal of NA–PY through N—H···O and O—H···O hydrogen bonds. The existence of nicotinic acid in zwitterionic form renders the molecule highly polar thus making it susceptible to cocrystal formation. A further investigation is underway to address the question why and when NA becomes a zwitterion during cocrystal formation as pure NA is known to exist in non-zwitterionic form (Kutoglu & Scheringer, 1983). The topological analysis reveals that the NA–NA hydrogen bonds have a strong localization of electron density on their bond critical points which explains the reason for cocrystal formation and its robustness. This is correlated to the high kinetic energy and potential energy density at BCPs. This fact can also be the reason for the high-resolution diffraction by this cocrystal. The existence of these two strongest N—H···O interactions between the NA moieties suggests that the formation of the cocrystal should start with the formation of NA–NA dimers. This dimer subsequently interacts with the PY moieties. Other NA–*X* cocrystals are under study to better understand the leading role of NA in the formation of cocrystals.

Acknowledgements

The authors gratefully acknowledge the Higher Education Commission and the Federal Government of Pakistan for funding under the Public Sector Development Programme to establish the Materials Chemistry Laboratory at The Islamia University of Bahawalpur, Pakistan, which made this study possible. Special thanks to Dr Christian Jelsch, CRM2, Université de Lorraine, Nancy, France, for updating *MoPro* software on our request.

References

Abramov, Y. A., Brammer, L., Klooster, W. T. & Bullock, R. M. (1998). *Inorg. Chem.* **37**, 6317–6328.
Athimoolam, S. & Natarajan, S. (2007). *Acta Cryst.* E**63**, o963–o965.
Bader, R. F. (1998). *J. Phys. Chem. A*, **102**, 7314–7323.
Bader, R. F. W. (1990). *Atoms in Molecules: A Quantum Theory*. Oxford University Press.
Bankiewicz, B. & Wojtulewski, S. (2019). *Cryst. Growth Des.* **19**, 6860–6872.
Blöchl, P. E. (1994). *Phys. Rev. B*, **50**, 17953–17979.
Bond, A. D. (2007). *CrystEngComm*, **9**, 833–834.
Brittain, H. G. (2012). *Cryst. Growth Des.* **12**, 5823–5832.
Brock, C. P., Dunitz, J. D. & Hirshfeld, F. L. (1991). *Acta Cryst.* B**47**, 789–797.
Bruker (2016). *APEX3, SAINT* and *SADABS*. Bruker AXS Inc., Madison, Wisconsin, USA.
Budavari, S., O'Neil, M. J., Smith, A. & Heckelman, P. E. (1989). *The Merck Index*, 11th ed., pp. 2330–2331. Rahway, NJ: Merck.
Canner, P. L., Berge, K. G., Wenger, N. K., Stamler, J., Friedman, L., Prineas, R. J. & Friedewald, W. (1986). *J. Am. Collect. Cardiol.* **8**, 1245–1255.
Carlson, L. A. (2005). *J. Intern. Med.* **258**, 94–114.
Chopra, D., Cameron, T. S., Ferrara, J. D. & Guru Row, T. N. (2006). *J. Phys. Chem. A*, **110**, 10465–10477.
Chopra, D., Row, T. N. G., Arunan, E. & Klein, R. A. (2010). *J. Mol. Struct.* 964, 126–133.
Desiraju, G. R. (2003). *CrystEngComm*, **5**, 466–467.
Destro, R., Soave, R., Barzaghi, M. & Lo Presti, L. (2005). *Chem. Eur. J.* **11**, 4621–4634.
Dittrich, B., Hübschle, C. B., Luger, P. & Spackman, M. A. (2006). *Acta Cryst.* D**62**, 1325–1335.
Dittrich, B., Koritsánszky, T. & Luger, P. (2004). *Angew. Chem. Int. Ed.* **43**, 2718–2721.
Dittrich, B., Strumpel, M., Schäfer, M., Spackman, M. A. & Koritsánszky, T. (2006). *Acta Cryst.* A**62**, 217–223.
Dittrich, B., Weber, M., Kalinowski, R., Grabowsky, S., Hübschle, C. B. & Luger, P. (2009). *Acta Cryst.* B**65**, 749–756.
Dolomanov, O. V., Bourhis, L. J., Gildea, R. J., Howard, J. A. K. & Puschmann, H. (2009). *J. Appl. Cryst.* **42**, 339–341.
Domagała, S., Fournier, B., Liebschner, D., Guillot, B. & Jelsch, C. (2012). *Acta Cryst.* A**68**, 337–351.
Dominiak, P. M., Makal, A., Mallinson, P. R., Trzcinska, K., Eilmes, J., Grech, E., Chruszcz, M., Minor, W. & Woźniak, K. (2006). *Chem. Eur. J.* **12**, 1941–1949.
Du, J. J., Lai, F., Váradi, L., Williams, P. A., Groundwater, P. W., Platts, J. A., Hibbs, D. & Overgaard, J. (2018). *Crystals*, **8**, 46.
Du, J. J., Váradi, L., Williams, P. A., Groundwater, P. W., Overgaard, J., Platts, J. A. & Hibbs, D. E. (2016). *RSC Adv.* **6**, 81578–81590.
Duggirala, N. K., Perry, M. L., Almarsson, Ö. & Zaworotko, M. J. (2016). *Chem. Commun.* **52**, 640–655.
El Haouzi, A., Hansen, N. K., Le Hénaff, C. & Protas, J. (1996). *Acta Cryst.* A**52**, 291–301.
Espinosa, E., Molins, E. & Lecomte, C. (1998). *Chem. Phys. Lett.* **285**, 170–173.
Espinosa, E., Souhassou, M., Lachekar, H. & Lecomte, C. (1999). *Acta Cryst.* B**55**, 563–572.
Flaig, R., Koritsánszky, T., Soyka, R., Häming, L. & Luger, P. (2001). *Angew. Chem. Int. Ed.* **40**, 355–359.
Flierler, U., Stalke, D. & Farrugia, L. J. (2011). In *Modern Charge-Density Analysis*, pp. 435–467. Dordrecht: Springer.
Ford, S. J., McIntyre, G. J., Johnson, M. R. & Evans, I. R. (2013). *CrystEngComm*, **15**, 7576–7582.
Fournier, B., Bendeif, E. E., Guillot, B., Podjarny, A., Lecomte, C. & Jelsch, C. (2009). *J. Am. Chem. Soc.* **131**, 10929–10941.
Ghosh, T., Juturu, T., Nagar, S. N. & Kamath, S. (2021). In *Multidisciplinary Digital Publishing Institute Proceedings*, Vol. 62, No. 1, p. 12.
Giannozzi, O., Andreussi, T., Brumme, O., Bunau, M., Buongiorno Nardelli, M., Calandra, R., Car, C., Cavazzoni, D., Ceresoli, M., Cococcioni, N., Colonna, I., Carnimeo, A., Dal Corso, A., de Gironcoli, S., Delugas, P., DiStasio, A., Ferretti, A., Floris, G., Fratesi, G., Fugallo, R., Gebauer, U., Gerstmann, F., Giustino, T., Gorni, J., Jia, M., Kawamura, M., Ko, A., Kokalj, E., Küçükbenli,

M., Lazzeri, M., Marsili, N., Marzari, F., Mauri, F., Nguyen, H. V., Nguyen, A., Otero-de-la-Roza, L., Paulatto, S., Poncé, D., Rocca, R., Sabatini, B., Santra, M., Schlipf, M., Seitsonen, A., Smogunov, I., Timrov, T., Thonhauser, P., Umari, N., Vast, X., Wu, S. & Baroni, S. (2017). *J. Phys. Condens. Matter*, **29**, 465901.
Gille, A., Bodor, E. T., Ahmed, K. & Offermanns, S. (2008). *Annu. Rev. Pharmacol. Toxicol.* **48**, 79–106.
Grabowsky, S., Kalinowski, R., Weber, M., Förster, D., Paulmann, C. & Luger, P. (2009). *Acta Cryst.* B**65**, 488–501.
Grimme, S., Antony, J., Ehrlich, S. & Krieg, H. (2010). *J. Chem. Phys.* **132**, 154104.
Gryl, M., Cenedese, S. & Stadnicka, K. (2015). *J. Phys. Chem. C*, **119**, 590–598.
Guillot, B., Viry, L., Guillot, R., Lecomte, C. & Jelsch, C. (2001). *J. Appl. Cryst.* **34**, 214–223.
Hansen, N. K. & Coppens, P. (1978). *Acta Cryst.* A**34**, 909–921.
Hathwar, V. R., Pal, R. & Guru Row, T. N. (2010). *Cryst. Growth Des.* **10**, 3306–3310.
Hathwar, V. R., Thakur, T. S., Dubey, R., Pavan, M. S., Guru Row, T. N. & Desiraju, G. R. (2011). *J. Phys. Chem. A*, **115**, 12852–12863.
Housset, D., Benabicha, F., Pichon-Pesme, V., Jelsch, C., Maierhofer, A., David, S., Fontecilla-Camps, J. C. & Lecomte, C. (2000). *Acta Cryst.* D**56**, 151–160.
Jebas, S. R. & Balasubramanian, T. (2006). *Acta Cryst.* E**62**, o5621–o5622.
Jelsch, C., Guillot, B., Lagoutte, A. & Lecomte, C. (2005). *J. Appl. Cryst.* **38**, 38–54.
Jelsch, C., Pichon-Pesme, V., Lecomte, C. & Aubry, A. (1998). *Acta Cryst.* D**54**, 1306–1318.
Kamanna, V. S., Ganji, S. H. & Kashyap, M. L. (2009). *Int. J. Clin. Pract.* **63**, 1369–1377.
Karimi-Jafari, M., Padrela, L., Walker, G. M. & Croker, D. M. (2018). *Cryst. Growth Des.* **18**, 6370–6387.
Kavuru, P., Aboarayes, D., Arora, K. K., Clarke, H. D., Kennedy, A., Marshall, L., Ong, T. T., Perman, J., Pujari, T., Wojtas, Ł. & Zaworotko, M. J. (2010). *Cryst. Growth Des.* **10**, 3568–3584.
Khan, T., Halle, J. C., Simonnin, M. P. & Schaal, R. (1977). *J. Phys. Chem.* **81**, 587–590.
Koch, U. & Popelier, P. L. (1995). *J. Phys. Chem.* **99**, 9747–9754.
Koritsanszky, T., Flaig, R., Zobel, D., Krane, H. G., Morgenroth, W. & Luger, P. (1998). *Science*, **279**, 356–358.
Koritsanszky, T. S. & Coppens, P. (2001). *Chem. Rev.* **101**, 1583–1628.
Kutoglu, A. & Scheringer, C. (1983). *Acta Cryst.* C**39**, 232–234.
Latha, M. M., Novena, L. M., Athimoolam, S. & Sridhar, B. (2020). *J. Mol. Struct.* **1205**, 127578.
Lecomte, C., Guillot, B., Muzet, N., Pichon-Pesme, V. & Jelsch, C. (2004). *Cell. Mol. Life Sci. (CMLS)*, **61**, 774–782.
Li, X., Wu, G., Abramov, Y. A., Volkov, A. V. & Coppens, P. (2002). *Proc. Natl Acad. Sci. USA*, **99**, 12132–12137.
Madsen, A. Ø. (2006). *J. Appl. Cryst.* **39**, 757–758.
Malik, S. & Kashyap, M. L. (2003). *Curr. Cardiol. Rep.* **5**, 470–476.
Mallinson, P. R., Smith, G. T., Wilson, C. C., Grech, E. & Wozniak, K. (2003). *J. Am. Chem. Soc.* **125**, 4259–4270.
Mata, I., Alkorta, I., Molins, E. & Espinosa, E. (2010). *Chem. Eur. J.* **16**, 2442–2452.
McKinnon, J. J., Spackman, M. A. & Mitchell, A. S. (2004). *Acta Cryst.* B**60**, 627–668.
Medvedev, A. G., Mikhailov, A. A., Prikhodchenko, P. V., Tripol'skaya, T. A., Lev, O. & Churakov, A. V. (2013). *Russ. Chem. Bull.* **62**, 1871–1876.
Munshi, P. & Guru Row, T. N. (2005). *J. Phys. Chem. A*, **109**, 659–672.
Muzet, N., Guillot, B., Jelsch, C., Howard, E. & Lecomte, C. (2003). *Proc. Natl Acad. Sci. USA*, **100**, 8742–8747.
Nagy, P. I. & Takács-Novák, K. (1997). *J. Am. Chem. Soc.* **119**, 4999–5006.
Nguyen, T. H., Groundwater, P. W., Platts, J. A. & Hibbs, D. E. (2012). *J. Phys. Chem. A*, **116**, 3420–3427.
Nicolis, E., Lampronti, I., Dechecchi, M. C., Borgatti, M., Tamanini, A., Bianchi, N., Bezzerri, V., Mancini, I., Grazia Giri, M., Rizzotti, P., Gambari, R. & Cabrini, G. (2008). *Int. Immunopharmacol.* **8**, 1672–1680.
Owczarzak, A. & Kubicki, M. (2018). *Crystals*, **8**, 132.
Parsons, S., Flack, H. D. & Wagner, T. (2013). *Acta Cryst.* B**69**, 249–259.
Perdew, J. P., Burke, K. & Ernzerhof, M. (1996). *Phys. Rev. Lett.* **77**, 3865–3868.
Pichon-Pesme, V., Lecomte, C. & Lachekar, H. (1995). *J. Phys. Chem.* **99**, 6242–6250.
Popelier, P. (2000). *Atoms in Molecules. An Introduction.* Harlow: Prentice Hall.
Popelier, P. L. A. (1998). *J. Phys. Chem. A*, **102**, 1873–1878.
Prabha, E. A. J. Y., Kumar, S. S., Athimoolam, S. & Sridhar, B. (2017). *J. Mol. Struct.* **1129**, 113–120.
Prasad, R. V., Rakesh, M. G., Jyotsna, R. M., Mangesh, S. T., Anita, P. S. & Mayur, P. K. (2012). *Int. J. Pharm. Chem. Sci.* **1**, 725–36.
Qiao, N., Li, M., Schlindwein, W., Malek, N., Davies, A. & Trappitt, G. (2011). *Int. J. Pharm.* **419**, 1–11.
Sekhon, B. (2009). *Ars Pharm.* **50**, 99–117.
Sekhon, B. S. (2012). *DARU J. Pharm. Sci.* **20**, 45.
Sheldrick, G. M. (2015). *Acta Cryst.* C**71**, 3–8.
Sheldrick, G. M. (2014). *SHELXT 2014/5*. University of Göttingen, Göttingen, Germany.
Souhassou, M., Lecomte, C., Blessing, R. H., Aubry, A., Rohmer, M.-M., Wiest, R., Bénard, M. & Marraud, M. (1991). *Acta Cryst.* B**47**, 253–266.
Spackman, M. A. & Byrom, P. G. (1997). *Chem. Phys. Lett.* **267**, 215–220.
Spackman, M. A. & Jayatilaka, D. (2009). *CrystEngComm*, **11**, 19–32.
Stalke, D. (2011). *Chem. Eur. J.* **17**, 9264–9278.
Stalke, D. & Ott, H. (2008). *Nachr. Chem.* **56**, 131–135.
Steiner, T. (2003). *Crystallogr. Rev.* **9**, 177–228.
Takusagawa, F. & Shimada, A. (1976). *Acta Cryst.* B**32**, 1925–1927.
Thomas, S. P., Veccham, S. P. K., Farrugia, L. J. & Guru Row, T. N. (2015). *Cryst. Growth Des.* **15**, 2110–2118.
Turner, M. J., McKinnon, J. J., Wolff, S. K., Grimwood, D. J., Spackman, P. R., Jayatilaka, D. & Spackman, M. A. (2017). *CrystalExplorer17*. University of Western Australia.
Volkov, A., Messerschmidt, M. & Coppens, P. (2007). *Acta Cryst.* D**63**, 160–170.
Wright, W. B. & King, G. S. D. (1950). *Acta Cryst.* **3**, 31–33.
Zarychta, B., Pichon-Pesme, V., Guillot, B., Lecomte, C. & Jelsch, C. (2007). *Acta Cryst.* A**63**, 108–125.
Zhurov, V. V., Zhurova, E. A. & Pinkerton, A. A. (2008). *J. Appl. Cryst.* **41**, 340–349.